The baroclinic secondary instability of the two-dimensional shear layer

Jean Reinaud, Laurent Joly, Patrick Chassaing

The baroclinic secondary instability of the two-dimensional shear layer

Jean Reinaud and Laurent Joly
Department of Fluids Mechanics, E.N.S.I.C.A. Toulouse, 31056, France

Patrick Chassaing
Institut de Mécanique des Fluides de Toulouse, Toulouse, 31400, France

(Received 13 December 1999; accepted 19 June 2000)

The focus of this study is on the numerical investigation of two-dimensional, isovolume, high Reynolds and Froude numbers, variable-density mixing layers. Lagrangian simulations, of both the temporal and the spatial models, are performed. They reveal the breaking-up of the strained vorticity and density-gradient braids, connecting two neighboring primary structures. The secondary instability arises where the vorticity has been intensified by the baroclinic torque. A simplified model of the braid of the variable-density mixing layer, consisting of a strained vorticity and density-gradient filament, is analyzed. It is concluded that the physical mechanism responsible for the secondary instability is the forcing of the vorticity field by the baroclinic torque, itself sensitive to perturbations. This mechanism suggests a rapid route to turbulence for the variable-density mixing layer. © *2000 American Institute of Physics.* [S1070-6631(00)00810-2]

I. INTRODUCTION

Shear dominated binary mixing or thermal mixing processes arise in a large number of industrial and geophysical flows and their specific features have been extensively studied. As quoted by Turner[1] the density inhomogeneity yields the generation-destruction of vorticity by the baroclinic torque. This source term of the vorticity transport equation is due to the misalignment between the density gradient and the pressure gradient. Experimental evidence highlights the influence of the density gradient on the global behavior of incompressible, variable-density simple shear flow; see Brown and Roshko[2] and Konrad.[3] Lele[4] even suggested that the baroclinic torque may be invoked to explain the Mach number effect, together with dilatation, on the spreading rate of the compressible mixing layer.

Within the frame of the Boussinesq approximation, Staquet[5] performed numerical experiments on a stratified shear layer. During the development of the primary Kelvin–Helmholtz instability, the vorticity field reorganizes into large vortical cores linked by thin vorticity layers hereafter referred to as ''braids.'' The author confirmed and further analyzed the baroclinic secondary Kelvin–Helmholtz type instability, that was observed experimentally by Altman[6] in a tilted water channel. This secondary instability, emerging at the stagnation points of the vortical braids between the main Kelvin–Helmholtz structures was also suggested by Corcos and Sherman[7] and earlier hinted by Thorpe.[8] The study of such secondary instabilities is crucial as, according to Thorpe,[9] it could be one of the mechanisms that triggers turbulence in geophysical shear layers. The braids, subjected to baroclinic vorticity production, are continuously stretched, experiencing a strain rate roughly proportional to the circulation around the cores, see Corcos and Sherman.[7] The strain rate, shown to be Reynolds-number independent by Staquet,[5] has been invoked, conformly with the work of Dritschel *et al.*,[10] together with Richardson number effects, to explain the stability properties of the vorticity braid in the stratified mixing layer.

The theoretical work of Dritschel *et al.*[10] stressed the stabilizing effect of a uniform strain field on a uniform vorticity filament. The basic mechanism lies both on the spanwise thinning of the vorticity layer, decreasing the magnitude of perturbations, and a streamwise stretching, making the wavenumber of disturbances collapse to zero. The authors demonstrated that by considering the ratio of the strain rate γ to the vorticity ω, a value above 25% yields the result that any perturbation is damped, i.e., its amplitude can only decrease with time. For weaker values of the strain rate, the linear theory predicts that, after an initial growth, an infinitesimal disturbance reaches a maximum, the amplification being 3 with $\gamma/\omega=6.5\%$ and 6.55 with $\gamma/\omega=5\%$, and then finally decays. Thus, the maximum amplitude is shown to depend on the local ratio of the time scales associated with the strain and the vorticity $\gamma/\omega\sim\tau_\omega/\tau_\gamma$. But the amplitude of a perturbation, which is initially finite, reaches finite values, invalidating the linear approach (for example, the maximum amplification may be greater than 10^{81} if $\gamma/\omega<10^{-3}$). Taking into account the nonlinear effects, the authors concluded that roll-up can actually occur depending on the initial finite magnitude of the disturbance and the γ/ω ratio. The authors suggest that the ratio between the local straining and the local vorticity should provide a fair criterion to analyze the stability properties of stretched vorticity layers even in more complex situations. In the stably stratified mixing layer studied by Staquet[5] the baroclinic torque enhances vorticity in the braids such that the ratio γ/ω decreases, indicating the possibility of a secondary instability on the braid. In that case, the author proposes $\gamma/\omega=1.85\%$ and a Richardson number of 0.04 as empirical threshold values for the development of the secondary, baroclinic instability.

The focus of the present paper is on the effects of baroclinicity on the two-dimensional mixing layer beyond the Boussinesq approximation. This situation is likely to occur in the early, quasi-two-dimensional transition of low Mach number, high Reynolds, and Froude numbers shear flows. Soteriou and Ghoniem[11] have studied two-dimensional, high Reynolds and Froude numbers, incompressible, spatially developing, variable-density mixing layers using a Lagrangian approach adapted from the vortex method. Both the unforced and externally forced cases are investigated in their paper. The authors showed a good agreement between their numerical results and the semiempirical formulas summarized by Dimotakis[12] on the unforced shear layers. The spreading rate, the eddy convection speed and the entrainment ratio, directly connected to the Kelvin–Helmholtz structure development, are notably affected by the density ratio according to experimental data. The physical mechanism, distorting and moving the main vortical structures, is a direct consequence of the redistribution of vorticity. The baroclinic torque intensifies the vorticity on the light-side of the primary Kelvin–Helmholtz structures while it destroys vorticity on the heavy-side. While forcing the flow at the inlet, i.e., the trailing edge of the splitter plate, the authors showed the qualitative modification of the response of the layer, especially for the spreading rate. They suggest that the observed behavior is to be related to the orientation of the layer, known to depend on the velocity and density ratio, together with the finite amplitude of the forcing. The present contribution is a step further toward a better insight on the transition to turbulence of the forced plane mixing layer when submitted to a density stratification. Both models—the temporal shear layer and the spatially developing mixing layer—are investigated using an extension of the Blob Vortex Method called the Lagrangian Transport Element Method. The method, carrying both the vorticity and the density gradient, has been introduced by Anderson[13] and developed by Ghoniem *et al.*[14] The Lagrangian approach avoids the spatial discretization of the flow gradients and handles advection through the displacement of the elements, limiting the numerical diffusion, see Puckett.[15] This numerical method resolves the scales available from the spatial discretization without much diffusion while considering the smaller scales as a ''substructural phenomena,'' see Soteriou.[16] Hence, it yields a fair numerical tool to investigate Kelvin–Helmoholtz type instabilities known to be inviscid as quoted by Michalke.[17]

The focus of the present contribution is on the secondary instability of the variable-density mixing layer. The paper is organized as follows. Section II is devoted to the derivation of the numerical procedure. The numerical simulations of the temporal mixing layer are presented in Sec. III. A secondary Kelvin–Helmholtz type instability arises where the baroclinic torque has intensified the vorticity field. Validation issues are included and rely on comparisons with respect to semiempirical formulas available from experimental data of Brown[18] and Dimotakis.[12] Then, the physical mechanism is analyzed on a simple model of a uniformly strained, truncated density-gradient and vorticity sheet. The model allows for an estimation of the effects of the strain field on the stability properties of the vorticity braids in the variable-density mixing layer. Then, in Sec. IV, the spatial model of the shear layer is investigated and confirms the sensitivity of the vorticity braids to the baroclinic secondary instability. It is concluded, in Sec. V, that the baroclinic torque, while promoting the destabilization of vorticity braids, is central to the specific route toward turbulence of the variable-density mixing flows.

II. FORMULATION AND NUMERICAL SCHEMES

The evolution of a two-dimensional, variable density, isovolume, inviscid flow at the limit of infinite Froude number is investigated. The governing equations are

$$\boldsymbol{\nabla}\cdot\mathbf{u}=0, \tag{1}$$

$$\mathrm{d}_t\rho=0, \tag{2}$$

$$\mathrm{d}_t\mathbf{u}=-\frac{1}{\rho}\boldsymbol{\nabla}p, \tag{3}$$

where $\boldsymbol{\nabla}=(\partial./\partial x,\partial./\partial y)$ is the gradient operator, $\mathrm{d}_t=\partial./\partial t+\mathbf{u}.\boldsymbol{\nabla}$ is the material derivative, p the pressure, and ρ the density.

The equations can be recast in nonprimitive variables using the Helmholtz decomposition,

$$\mathbf{u}=\mathbf{u}_\omega+\mathbf{u}_p, \tag{4}$$

$$\mathbf{u}_p=\boldsymbol{\nabla}\phi, \tag{5}$$

$$\Delta\phi=0, \tag{6}$$

$$\mathbf{u}_\omega=\boldsymbol{\nabla}\times\psi, \tag{7}$$

$$\Delta\psi=-\omega, \tag{8}$$

$$\mathrm{d}_t\omega=\mathrm{d}_t\mathbf{u}\times\frac{\boldsymbol{\nabla}\rho}{\rho}, \tag{9}$$

$$\mathrm{d}_t\boldsymbol{\nabla}\rho=-{}^t[\boldsymbol{\nabla}\mathbf{u}].\boldsymbol{\nabla}\rho, \tag{10}$$

where $\mathbf{u}_p$ is the potential velocity field, ϕ the velocity potential, $\mathbf{u}_\omega$ the solenoidal velocity field, ψ the stream function and ω is the vorticity. Thus the solenoidal field can be obtained by the Biot–Savart integral from the vorticity distribution.

Following Ghoniem *et al.*,[14] the so-called ''Blob Vortex Method'' originated by Chorin[19] can be generalized to perform simulations of variable-density flows. The numerical procedure aims at tracking a collection of n Lagrangian elements transporting both the local value of the vorticity and the density gradient on a radially symmetric core, characterized by its shape, the ''cut-off'' function f_δ, and its radius, the ''cut-off'' parameter δ. Thus δ can be seen as the scale beyond which fluctuations are locally averaged, see Soteriou and Ghoniem,[16] Lundgren *et al.*[20] The cutoff functions used in this study have been proposed by Beale and Majda.[21] They rely on Gaussian functions and lead to a second-order accuracy for the velocity field, hereafter referred to as $K2$, or a fourth-order one, $K4$:

$$(K2)f_\delta(r)=\frac{1}{\pi\delta^2}\exp\left(-\frac{r^2}{\delta^2}\right), \tag{11}$$

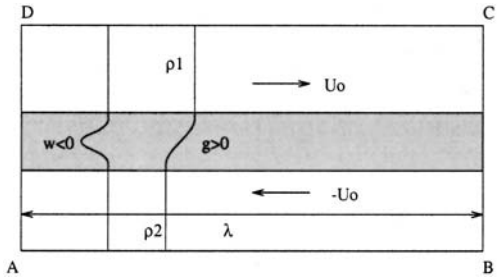

FIG. 1. Geometry of the temporal model (g stands for the density gradient $\nabla\rho$).

$$(K4)f_\delta(r)=\frac{1}{\pi\delta^2}\left(2\exp\left(-\frac{r^2}{\delta^2}\right)-\frac{1}{2}\exp\left(-\frac{r^2}{2\delta^2}\right)\right). \quad (12)$$

The n elements are initially defined as the grid points of a uniform Cartesian mesh with size h. The basic equations are the Lagrangian vortex element displacement,

$$\mathrm{d}_t\mathbf{x}_i=\mathbf{u}(\mathbf{x}_i,t) \quad (13)$$

coupled with the regularized Biot–Savart summation

$$\mathbf{u}_\omega(\mathbf{x},t)=\int\int K_\delta(\mathbf{x}-\mathbf{x}')\omega(\mathbf{x}',t)\mathrm{d}\mathbf{x}', \quad (14)$$

where $K_\delta=K*f_\delta$ is the convolution product between the kernel of the Biot–Savart integral K and the ''cut-off''—or desingularization—function f_δ, and the vorticity transport equation (9). They are evolved in time simultaneously using Runge–Kutta schemes, a fourth-order one referred to as RK4, or second order named RK2. The determination of the potential field depends on the boundary conditions and this will be introduced in Sec. III for the temporal model and in Sec. IV for the spatially developing flow. Both the acceleration and the density gradient fields have to be updated at each calculation step. The acceleration of the transport elements is obtained by a second-order backward finite difference scheme. The transport equation of the density gradient (10) is written in an alternative form available from Heidarinejad.[22] In this equation, the density gradient is deduced from the local stretching of an isopycnic line according to

$$\frac{|\nabla\rho|}{|\mathrm{d}l|}=cst \text{ and } \nabla\rho\cdot\mathrm{d}l=0. \quad (15)$$

In the discrete description of the flow map, the local stretching around an element is obtained from the distance with the neighboring elements within the same isopycnic line. Then, by noting that

$$\Delta\rho=\nabla\cdot\nabla\rho, \quad (16)$$

the density field can be obtained using the reconstruction formula, see Anderson,[13]

$$\rho(\mathbf{x},t)=\int\int L_\delta(\mathbf{x}-\mathbf{x}')\cdot\nabla\rho(\mathbf{x}',t)\mathrm{d}\mathbf{x}'+\rho_p, \quad (17)$$

where ρ_p is a ''potential'' density depending on the boundary conditions and $L_\delta=L*f_\delta$ is the desingularized gradient of the two-dimensional Green function with

$$L(\mathbf{x})=\frac{1}{2\pi r^2}(x,y). \quad (18)$$

A Lagrangian spatial refinement strategy originated in Ghoniem *et al.*,[14] which inserts or removes elements along isopycnic lines, is adopted and ensures the required overlapping between neighboring blobs, see Leonard.[23]

III. THE TEMPORAL MODEL

A. The geometry and initial conditions

The temporal layer can be viewed as a mathematical idealization of a mixing layer developing downstream of a splitter plate. It results from the Galilean transformation $x=U_m*t$, where $U_m=(U_1+U_2)/2$ is the mean velocity between the two free streams of the targeted spatially evolving flow. The model becomes strictly valid if the mean velocity is much larger than half the velocity difference $\Delta U/2=(U_1-U_2)/2=U_0$, Rogers and Moser.[24] Nevertheless, even for lower velocity ratios, the temporal model is expected to reveal the main dynamic mechanisms of the spatially developing mixing layer, Metcalfe *et al.*,[25] Rogers and Moser.[24] In that model, the computational domain follows the time evolution of a single wavelength λ, observed in a reference frame moving at U_m. Hence, it suffers from the streamwise periodization of an otherwise quasiperiodic flow, but it reduces drastically the computational load. The initial condition is a standard Gaussian negative vorticity layer on which a density gradient layer of the same thickness is superimposed. This choice is in good agreement with the experimental mean velocity and density profiles near the trailing edge of a plane splitter plate, from Brown and Roshko,[2]

$$\omega(y)=-\frac{\Delta U}{\pi^{1/2}\sigma}\exp\left(-\frac{y^2}{\sigma^2}\right), \quad (19)$$

$$\nabla\rho(y)=\begin{pmatrix}0\\ \dfrac{\rho_1-\rho_2}{\pi^{1/2}\sigma}\exp\left(-\dfrac{y^2}{\sigma^2}\right)\end{pmatrix}. \quad (20)$$

Periodicity is assumed in the streamwise direction and is set to the most unstable wavelength of the uniform density case $\lambda=13.2\sigma$, Michalke,[26] where σ is the standard deviation of the initial vorticity profile that measures the thickness of the layer. This value is used in the variable-density computations for which Soteriou and Ghoniem[11] have shown that the most unstable wavelength depends weakly on the density ratio.

The geometry of the flow is described in Fig. 1. The problem is normalized by the velocity scale $\Delta U/2=U_0$, the density ρ_1 of the upper flow, and the length scale σ. The periodic boundary condition is treated as an exact summation of the velocity field induced by any vortex in the computation domain and its infinite row of images in the other periods (Ghoniem *et al.*[14]). The equations are solved with the RK4 scheme and the cut-off function is $K4$. At $t=0$ the flow is perturbed. The perturbation consists of a crosswise displacement of the elements according to a sinewave whose wavelength is $\lambda=13.2\sigma$, i.e., the length of the domain. The magnitude of the sinewave superimposed on the location of

TABLE I. Description of the computations for the investigation of the temporal mixing layer. The sixth column gives the number of isopycnic lines simulated. Simulations of mixing layers with a density ratio greater than unity have not been performed as, in the temporal model, cases with $\rho_2/\rho_1=s$ and $s'=1/s$ are symmetric.

Run	ρ_2/ρ_1	h	δ	dt	Isopycnic
T1a	1	0.2	0.25	0.1	19
T1b	1	0.1	0.125	0.1	37
T2	1/2	0.2	0.25	0.1	19
T3a	1/3	0.2	0.25	0.1	19
T3b	1/3	0.1	0.125	0.1	37
T3c	1/3	0.05	0.0625	0.1	73
T3d	1/3	0.1	0.125	0.05	37
T3e	1/3	0.1	0.125	0.2	37
T3f	1/3	0.15	0.1875	0.1	25
T4	1/4	0.2	0.25	0.1	19
T5	1/5	0.2	0.25	0.1	19
T6	1/6	0.2	0.25	0.1	19

the elements is 1% of λ. It should be noted that, within this context, the pairing of two primary structures is prevented.

Even for a variable density situation, the circulation over a period is demonstrated to remain constant and depends on the length of the period and the velocity of the two free streams. Considering the rectangular closed contour over a period ($\mathcal{C}=$ABCD) defined in Fig. 1, the circulation is

$$\Gamma_0=\int_{\mathcal{C}}\mathbf{u}.d\mathbf{l}=\int_A^B\mathbf{u}.d\mathbf{l}+\int_B^C\mathbf{u}.d\mathbf{l}+\int_C^D\mathbf{u}.d\mathbf{l}+\int_D^A\mathbf{u}.d\mathbf{l}.$$

Because of the streamwise periodicity condition, velocity profiles along BC and AD are equal and the sum of the two related integrals is null. Moreover along the two segments AB and CD placed in the free streams, the velocity is uniform ($\pm U_0$). Consequently, the circulation over the period is $\Gamma_0=-2\lambda U_0=-\lambda\Delta U$.

Thus, whatever the amount of circulation created somewhere in the domain by the baroclinic torque, it is removed elsewhere within the same period.

Table I gives the description of the runs performed for the investigation of the temporal mixing layer. They differ by the density ratio or the spatial resolution.

B. The primary Kelvin–Helmholtz instability

As illustrated in Fig. 2 from the vortex element position, a primary Kelvin–Helmholtz instability is developing. During the roll-up, the so-created vortical core induces a strain field on the braid. Then the fluid from the braid experiences an acceleration that advects it toward the vortical core, in opposite direction on both sides of the saddle point of the braid. Coupled with the local density gradient, of uniform sign along the braid, vorticity is consequently both produced and removed. The sign of the baroclinic torque contribution to the vorticity field, set by the density gradient, is such that vorticity is created in the light-side braid of the main structure and destroyed inside the heavy-side braid. As noted in the previous section the circulation over a period remains constant.

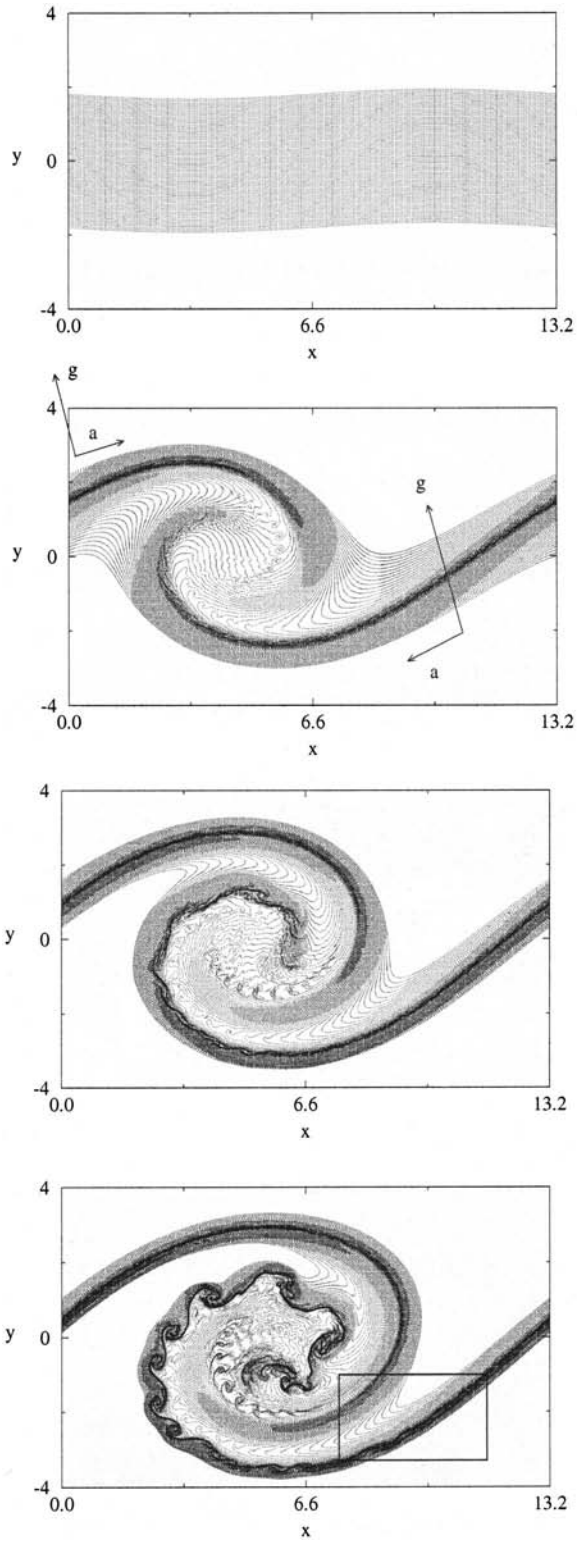

FIG. 2. Location of the elements at $t=0$, $t=17$, $t=20$, and $t=22$ for the variable-density temporal mixing layer with $\rho_1/\rho_2=3.0$ (run T3c). g stands for $\nabla\rho$ and a for the acceleration, indicating the sign of the baroclinic production of vorticity. The box on the bottom figure indicates the location of the close-up to be presented in Fig. 8.

The temporal evolution of the reduced circulation over the period is presented in Fig. 3(a) for the run T3c. In the presented result, the departure of the relative circulation from its expected constant value is kept under 1.5% until $t=22.0$

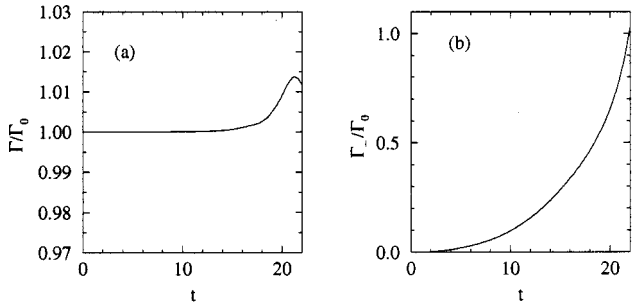

FIG. 3. (a) Time evolution of the reduced circulation over a period and (b) reduced negative created circulation for $\rho_1/\rho_2=3.0$ (run T3c). Γ_0 is the nondimensional initial circulation (-26.4 in normalized units).

while the baroclinic torque has created (from $t=0$) an amount of negative circulation Γ^- of the same order as the initial one $\Gamma_0=-\lambda\Delta U$ [see Fig. 3(b)]. Such significant productions of negative, and correspondingly positive circulation clearly suggest that the density stratification will have a significant influence on the flow.

The evolution of the vorticity field along the central isopycnic line (at $\rho=2.0$ and a density ratio $\rho_2/\rho_1=1/3$) at the early stage of the roll-up ($t=16.0$) is shown in Fig. 4. The vorticity distribution is seen to be essentially linear, and to exhibit vorticity oscillations in the high magnitude negative vorticity part. This point will be extensively discussed in the next section. It should also be noted that vorticity even reaches positive values.

Soteriou and Ghoniem[11] suggested that the positive and negative vorticity that is created can be described as a dipole superimposed on the reference vortex core of the uniform-density Kelvin–Helmholtz instability. This dipole then induces a convection velocity on the eddy such that the main structures are not advected at the mean velocity as it is the case in the uniform density situation. As seen before, the circulation of each vortex of that superimposed dipole may

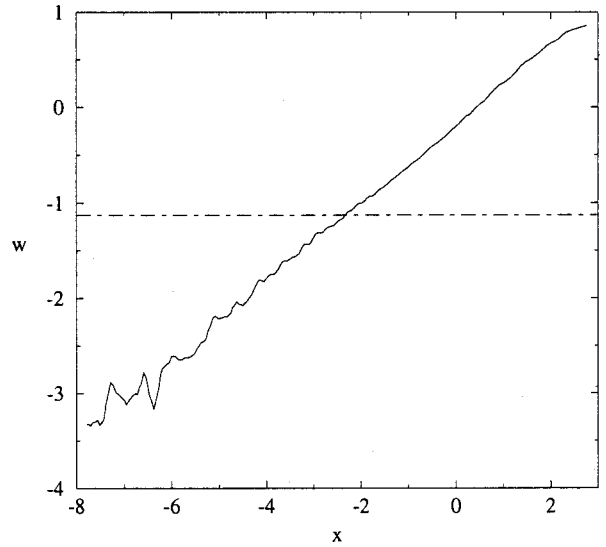

FIG. 4. Evolution of the vorticity along the central isopycnic line of the braid (run T3c at $t=16.0$). The solid line is for the computed profile. The dotted–dashed line marks the initial vorticity level.

TABLE II. Normalized eddy convection speed for the temporal model (numerical values and prediction by Brown's formula). The Poisson's equation is solved on a Cartesian mesh with $h=0.1$.

Run	ρ_2/ρ_1	U_c^t (Num.)	U_c^t (Brown)
T2	1/2	0.18	0.17
T3a	1/3	0.28	0.27
T4	1/4	0.33	0.33
T5	1/5	0.38	0.38
T6	1/6	0.41	0.42

be of same order of magnitude as that of the main structures. Brown,[18] proposed a semiempirical estimation of the eddy convective speed, consistent with the temporal model, that can be written as

$$U_c^t=U_c-U_m=1-2\frac{s^{1/2}}{1+s^{1/2}}, \tag{21}$$

where $s=\rho_2/\rho_1$ is the density ratio and U_c^t is the eddy convection speed in the reference frame of the temporal model (moving at U_m). This convection velocity is measured here from the displacement of the center of the structure. The center position is obtained by solving Poisson's equation on a Cartesian mesh and searching for the local extremum of the stream function.

The results are presented in Table II and summarized in Fig. 5. They show a good agreement with Brown's formula (21).

In agreement with the analysis of Soteriou and Ghoniem,[11] the baroclinic additional vorticity also breaks the symmetry of the entrainment, favoring the entrainment of the light fluid. Due to incompressibility, the loss of symmetry leads to the displacement of the structure toward the low-density stream.

The present results are compared to the proposal of Brown[18] in order to check the dependence of the spreading rate on the density ratio. In the reference frame moving at U_m, the thickness of the structure is seen to be independent of the density ratio, but the corresponding spatial spreading rate changes since the convective velocity is density-ratio

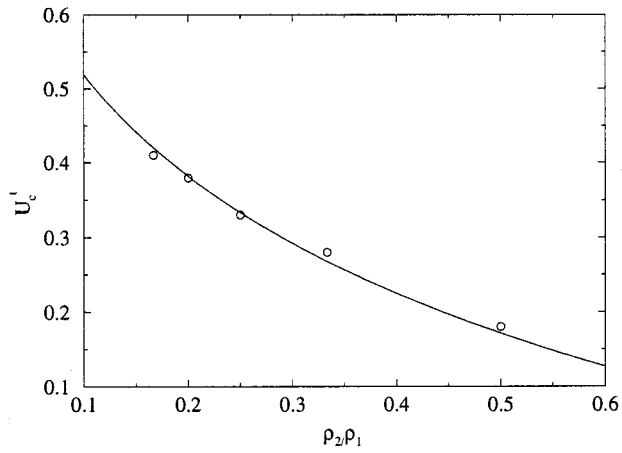

FIG. 5. Eddy convection speed for the temporal mixing layer; Brown formula (solid line), and numerical results (circles).

TABLE III. Effect of the density variation on the temporal spreading rate of the layer (δ is the maximum thickness of the structure over the period).

Run	ρ_1/ρ_2	$d\delta/dt$
T1a	1/1	0.267
T2	1/2	0.267
T3a	1/3	0.271
T4	1/4	0.274
T5	1/5	0.274
T6	1/6	0.269

sensitive. The total thickness of the structure is measured to the maximum spanwise distance between the two isopycnic lines departing from the free stream density by 1.1%. The slope of the temporal evolution of this thickness is obtained by a linear regression in the first linear range, i.e., before the saturation of the primary mode.

The slope measurements, presented in Table III are confirmed to be independent of the density ratio.

The strain field in the saddle point region that results from the roll-up of the main structure is illustrated in Fig. 6 for the passive scalar and the $s=1/3$ mixing layer. The strain rate γ, defined as $\gamma=|\nabla\mathbf{u}\cdot\eta|$, where η is the local tangent to the isopycnic line, exhibits a plateau around the saddle point. In this region, the strain field has been weakly altered by the density stratification. The normalized magnitude of the mean strain rate γ (see dashed and dotted lines) is found to be 0.225. This is consistent with the proposal of Corcos and Sherman[7] that the strain field between main Kelvin–Helmholtz cores is roughly proportional to the core circulations. In the present cases, within each core the baroclinic production is neutralized by a corresponding destruction of circulation. The strain around the saddle point is thus expected to remain unaffected by the density variation. In the uniform-density case, it can be noticed that the strain field decreases linearly close to the core with slope ± 0.043. Besides, the strain rate for the variable-density case reveals high magnitude fluctuations, with even changes of sign, near the vortical core. They are relevant to the secondary instabilities that are developing along the braid, a point extensively discussed in the next section. The temporal evolution of the strain rate at the saddle point is illustrated in Fig. 7 for the uniform-density case. It shows that the strain rate is roughly constant after $t\sim 17.0$, when most of the circulation is in the core, corresponding to the saturation of the primary Kelvin–Helmholtz instability.

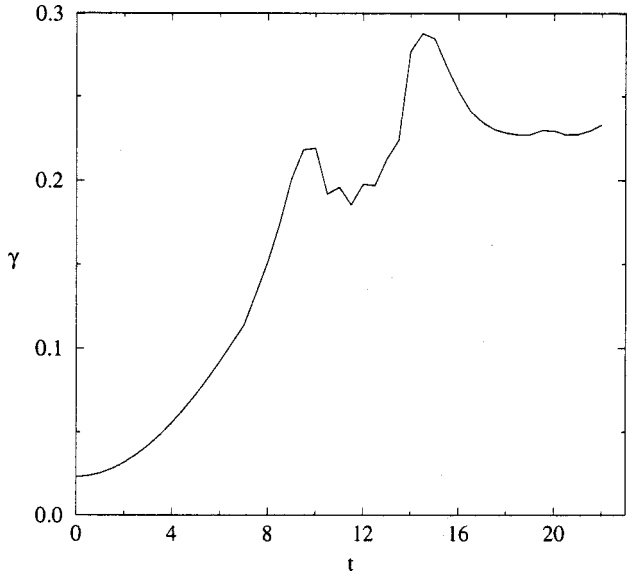

FIG. 7. Run T1b: time evolution of the strain at the saddle point.

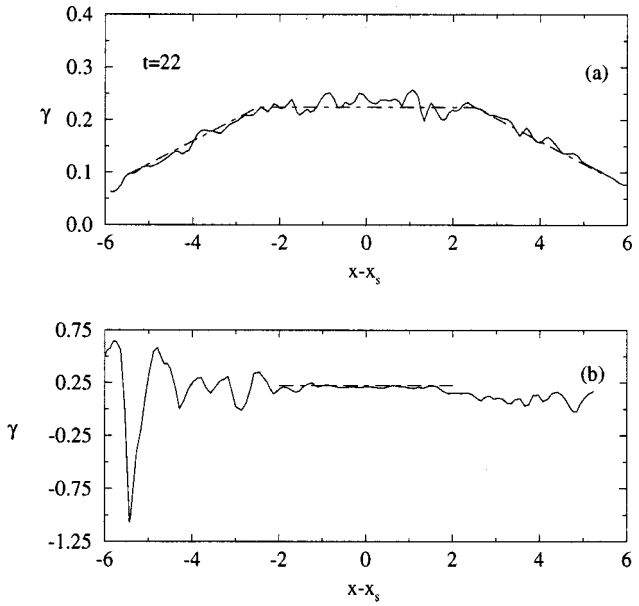

FIG. 6. The strain rate profile along the central isopycnic line of the braid; (a) run T1b, passive scalar, (b) run T3b, $s=1/3$ at $t=22.0$ (plotted only around the saddle point). Solid line shows the computed values. Dashed and dotted lines are suggesting the trends. x_s is the coordinate of the saddle point.

C. The evidence of a secondary instability

Figure 2 shows the locations of the vortex elements at $t=17$ and $t=22$ for the temporal variable-density mixing layer with $\rho_1/\rho_2=3.0$ for the most spatially resolved simulation (run T3c). It is shown that, on the braid side which experiences a baroclinic supply of vorticity, the vorticity sheet breaks up into a row of growing secondary structures. These structures are Kelvin–Helmholtz type structures and are growing both in time and space. They are clearly distinguishable from the curved vorticity layer surrounding the core but they are initiated backward in the favored braid.

Close to the saddle point, the isopycnic lines exhibit a wavy feature whose amplitude increases as the layer moves closer to the core, as seen in the close-up in Fig. 8. These oscillations are used to measure the wavelength λ_2 of the secondary mode at $t=22$. The actual shape of the central isopycnic line (x,y) is compared with a smoothed curve obtained by a sixth order nonlinear regression (x,y_r). In Fig. 9, the difference $(\Delta y=y-y_r)$ between the two curves is plotted along the mean line vs the associated curvilinear coordinate (s). The curve shows that the amplitude of oscillations is higher on the side of the isopycnic line where vorticity has been intensified (on the left-hand side), stressing the central

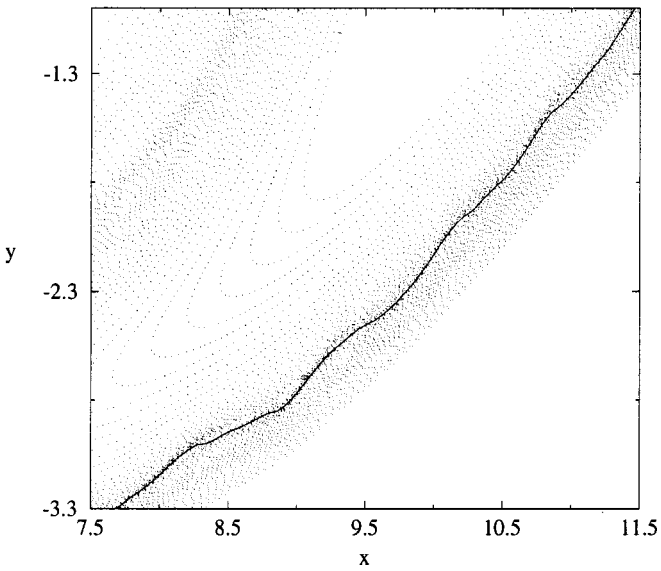

FIG. 8. Close-up from Fig. 2; location of the elements at $t=22.0$ (dots) for the variable-density temporal mixing layer (run T3c) and isopycnic line at $\rho=2.0$ (solid line).

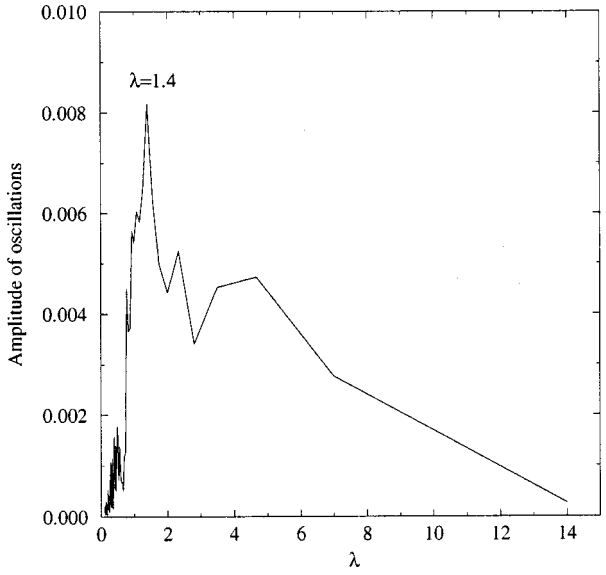

FIG. 10. Measurement of the wavelength of the secondary mode. Spectrum of the oscillations of the central isopycnic line in the braid ($\rho=2.0$) (run T3c) at $t=22.0$.

influence of ω. These undulations can be linked to the previously noted fluctuations of the vorticity distribution along the isopycnic lines. A spatial Fourier transform is performed on the curve $\Delta y=f(s)$ and the resulting spectrum is presented in Fig. 10. The main peak in the spectrum indicates a wavelength of oscillations $\lambda_2=8\sigma_l(t=22)$, where $\sigma_l(t=22)$ is the local thickness of the strained vorticity braid (here $\sigma_l\simeq\sigma/6$). This is consistent with the visually estimated separation between the small scale secondary roll-ups. The value does not correspond to the most unstable mode of the unstretched vorticity layer, i.e., $\lambda=13.2\sigma$. This point is examined in the following paragraph.

The temporal evolution of the perturbations along the braid is also investigated. The crosswise velocity fluctuations are analyzed along the central isopycnic line in the range $18<t<22$. The spatial spectra, presented in Fig. 11, illustrate two main features of the secondary roll-up. The first one is the amplification of the main mode. The second one is the continuous displacement of the main peak toward higher wavelengths, due to the stretching of the material, isopycnic lines. This point is confirmed since the temporal displacement of the main mode compares favorably with the strain rate γ, measured around the saddle point region. Considering a material segment $d\mathbf{l}$ submitted to the strain rate γ, the temporal evolution of its length is exponential as it is governed by the kinematic equation,

$$\frac{Dd\mathbf{l}}{Dt}=[\nabla\mathbf{u}].d\mathbf{l}, \tag{22}$$

so that as far as the wavelength of the main mode $\lambda_m(t)$ along the stretched braid is concerned, its temporal displacement can be expressed by

$$\frac{1}{\Delta t}\ln\left(\frac{\lambda_m(t+\Delta t)}{\lambda_m(t)}\right)=\gamma. \tag{23}$$

The result between $t=18$ and $t=22$ for the central isopycnic line are consistent with $\gamma\simeq0.225$ for that range of time and $(1/\Delta t).\ln(\lambda_m(22)/\lambda_m(18))=0.223$. Due to incompressibility, the thickness of the vorticity braid decreases as it is stretched. Thus, the local thickness of the vorticity profile σ_l decreases with time, while the wavelength of the oscillations λ_2 increases. Consequently, the ratio of $\lambda_2(t)$ to $\sigma_l(t)$ increases. The strained braid may eventually develop a secondary instability before reaching the most unstable λ to σ ratio, as is the case here.

During the secondary roll-ups, as during the primary one, elements of the newly-formed, thin braids are advected toward the secondary cores. Again, this acceleration, coupled with the density gradient, produces vorticity. Then the local topology of the vorticity field of a small scale structure shows some similarity with the one of the primary structure as illustrated on the isovorticity lines from Fig. 12. In both cases, the vortical core is surrounded by two braids, one with positive vorticity, on the heavy side of the core, and the other one experiencing a supply of negative vorticity. It is then conjectured that, because of these common features, a third

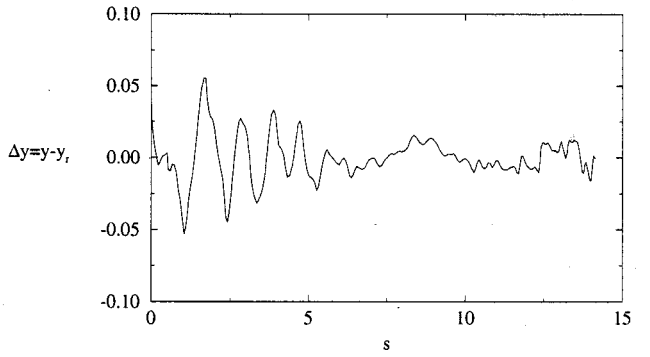

FIG. 9. Oscillations of the central isopycnic line ($\rho=2.0$) vs the curvilinear abscissa s (run T3c) at $t=22.0$.

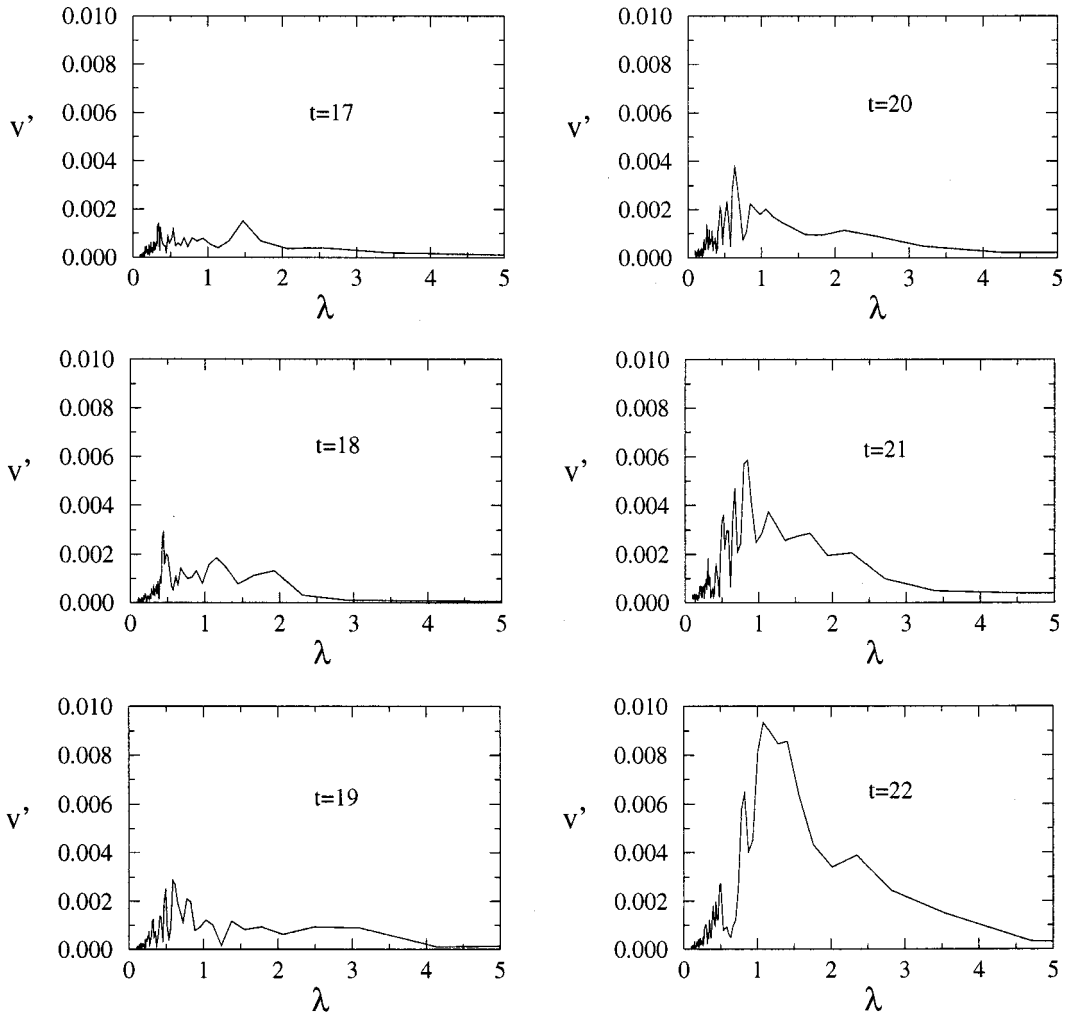

FIG. 11. Time evolution of the spectrum of the crosswise velocity fluctuations along the central isopycninc line in the range $18<t<22$ for the run (T3c).

generation of smaller baroclinic structures may appear, repeating the previous scenario. These structures have not been observed because they are beyond the scope of the spatial resolution. This baroclinic mechanism, creating smaller and smaller scales could provide a specific route to turbulence for the variable-density mixing layer.

As previously noted in Reinaud *et al.*,[27] the computational parameters, h and dt, influence the observed secondary instability as it is the response of a strongly unstable region of the flow submitted to a low-amplitude numerical noise. This influence is now briefly illustrated.

The crosswise velocity fluctuations that measure the local perturbations feeding the secondary mode are seen to depend indeed on the time step as seen from their spectra in Fig. 13(a). However, the enstrophy spectra at $t=15$ and $t=21$ are presented in Fig. 14(a) for the runs T3b, T3d, and T3e. It is seen that the time step has no significant influence on the range of solved scales that spread well beyond the baroclinic mode wave number k_{λ_2}. This suggests that, within this range of time steps, the numerical diffusion due to the temporal schemes does not prevent the development of the scales associated with the secondary instability.

The influence of the spatial discretization is also examined. The enstrophy spectra for the runs T3a, T3b, T3c, and T3f are presented in Fig. 14(b). The result clearly shows that the spatial scales available from the simulation are directly linked to the ''cut-off'' parameter δ. Again, as seen in Fig. 13(b), the oscillations of the braid that feed the secondary instability depend on the spatial discretization, coarser spatial discretizations favoring higher wavelengths. Nevertheless, all runs show the occurrence of the secondary instabilities, since the scales beyond k_{λ_2}, feeding the instability, are not damped by the spatial discretization. Thus, the simulations are able to catch the strongly unstable nature of the braid responding to a numerics-dependent perturbation. The central point is then to understand the physical mechanisms responsible for the unstable nature of the vorticity enhanced braid, since flow-dependant perturbations will end with the same result.

D. Variable-density vs uniform density mixing layers

In order to stress the specific aspects of the variable-density mixing layer, it is further analyzed vs the uniform density one (Runs T3b and T1b).

The development of the previously described small scale

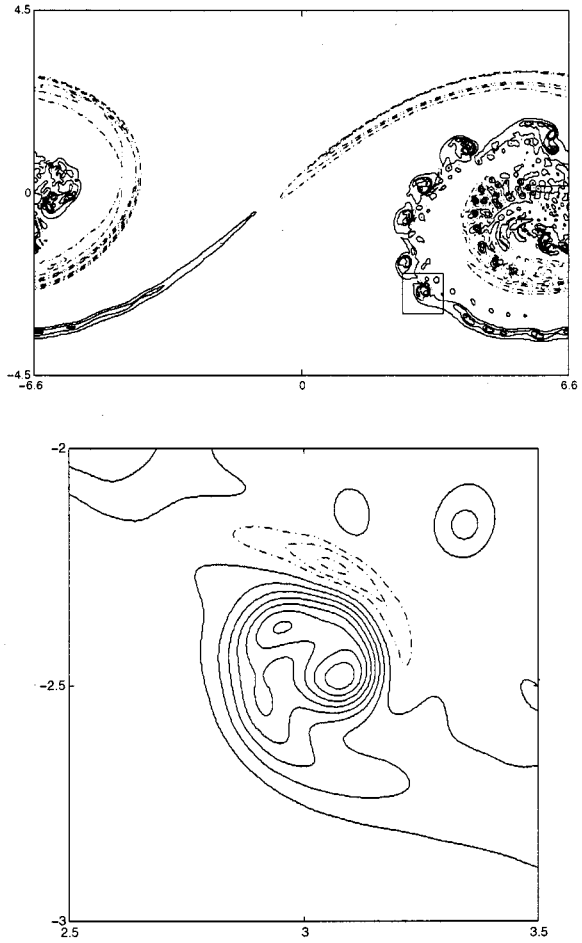

FIG. 12. Isovorticity lines with negative values of ω (solid lines) within the range $\omega=-9--1$ and positive value within the range 0.1–0.9 (dashed–dotted line). The box on the top figure shows the close-up frame presented on the bottom figure.

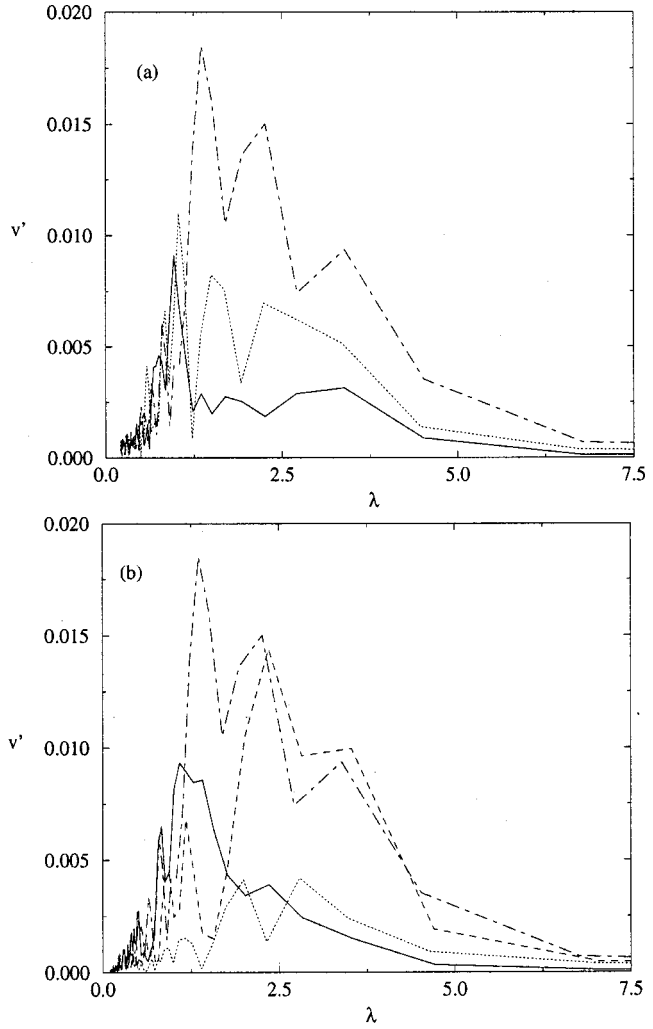

FIG. 13. Spectra of the crosswise velocity fluctuations along the vorticity braids at $t=22$. (a) Influence of the time step. Runs T3e (dotted), T3b (dotted–dashed), and T3d (solid line). (b) Influence of the spatial discretization. Runs T3a (dotted), T3f (dashed), T3b (dotted–dashed) and T3c (solid line).

structures has an influence on the overall growth rate of perturbations defined as

$$\frac{d\ln(I)}{dt}=\frac{d}{dt}\ln\left(\int_{\text{Domain}}|\mathbf{u}(\mathbf{x})-U(\mathbf{x})|d\mathbf{x}\right), \tag{24}$$

where U is the unperturbed velocity profile. The temporal evolution of $\ln(I/I_0)$ is shown in Fig. 15 for the variable-density mixing layer and the uniform-density case, where I_0 is the initial perturbation induced by the displacement of the elements. The graph shows a common standard 0.2 slope for $0<t<10$, see Ghoniem *et al.*[14] for the uniform density case. Then, the growth of the instability is significantly higher in the variable density case. During the development of the secondary small scale structures in the variable density case ($t>18$), the growth of the perturbations exhibits a 0.083 slope. This slope is more than twice the slope observed in the uniform-density case, 0.032.

Comparison between the magnitudes of the crosswise oscillations along the central line of the braid is also considered for the two cases. The standard deviation σ_y of the crosswise coordinate y relative to the mean curve obtained by the sixth order polynomial regression y_r is growing as illustrated by Fig. 16. Starting at a comparable level from $t=16.0$, undulations of the braid are shown to be much higher in the variable-density case; at $t=22$, $\sigma_y(s=1/3)/\sigma_y(s=1)=2.9$. Both the growth of the velocity departure from its initial field, and the steep increase of the crosswise oscillations demonstrate the specific instability of the variable-density mixing layer when compared to its passive scalar equivalent.

An additional simulation of a double period of the temporal mixing layer, including the forcing of the pairing mode has been performed and previously published, see Reinaud *et al.*[27] The results, not reproduced here, demonstrated that small scale break-up of the curved layer where vorticity has been intensified by the baroclinic torque and the development of the pairing mode are not exclusive phenomena. Nevertheless, this does not guarantee the existence of the small scale mode in the case of a spatially developing mixing layer. It is concluded that a similar investigation on the spatially developing variable-density mixing layer remains of central interest. The mechanisms that trigger the secondary break-up has also to be clarified.

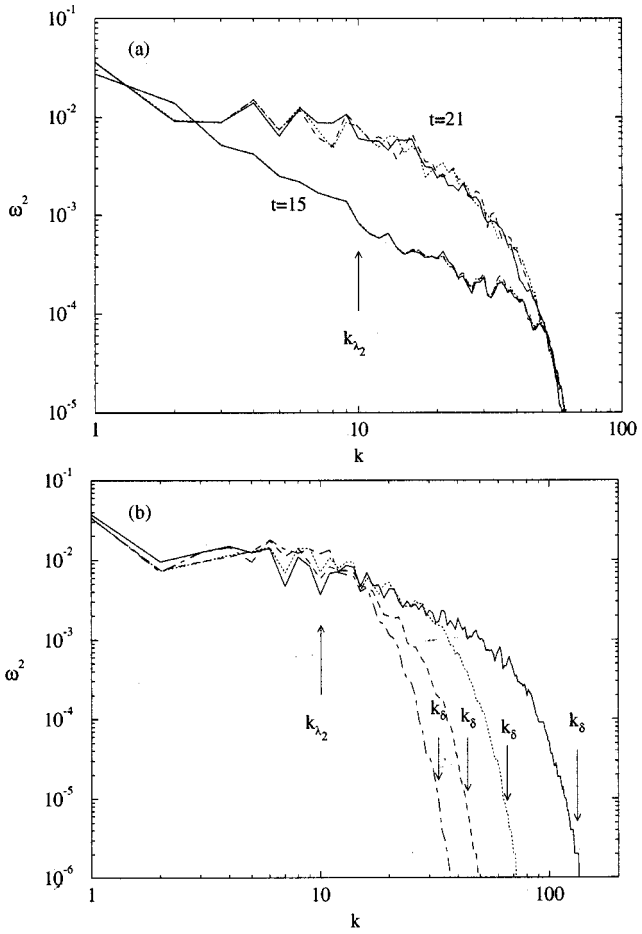

FIG. 14. Enstrophy spectra. (a) Influence of dt, at $t=15$ and $t=21$ for the runs T3e (dotted), T3b (dashed), and T3d (solid line). (b) Influence of h at $t=22$ for the runs T3a (dotted–dashed), T3f (dashed), T3b (dotted), and T3c (solid line). k_{λ_2} indicates the wave number associated with the secondary mode for the run T3c and k_δ indicates a wave number associated with $\delta=\lambda/1.6\,\delta=\lambda/2h$.

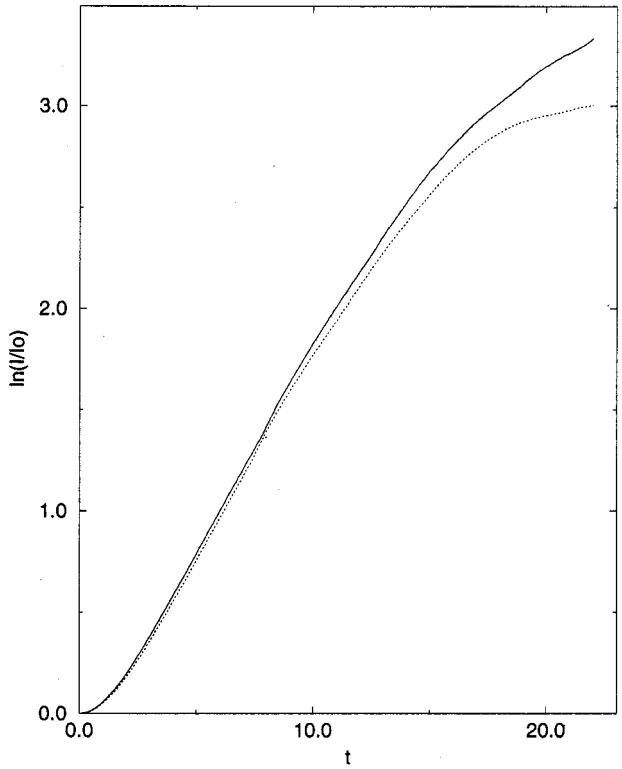

FIG. 15. Growth of the perturbation $\ln(I/I_0)$ over a period of the temporal model for run T3b, $\rho_1/\rho_2=3.0$ (solid line) and run T1b, $\rho_1/\rho_2=1.0$ (dotted line). $h=0.1$ in the two cases.

E. A simple model for the baroclinic vorticity braid

A simplified model of the stretched braid is now proposed. As seen previously (see Fig. 6), the strain is roughly uniform in the neighborhood of the saddle point of the braid. Furthermore, the strain remains rather unchanged after the development of the primary Kelvin–Helmholtz structures. Hence, the behavior of a uniform, infinite, vorticity, and density-gradient line at $y=0$ submitted to a uniform strain field $(u,v)=(\gamma x,-\gamma y)$ is relevant to mixing layer braids. Let ω_0 the vorticity, g_0 the density gradient, and ρ_0 the density define the initial conditions of that simplified model. Let us consider, without loss of generality, that $\omega_0<0$ and $g_0>0$. The velocity $\mathbf{u}$ is split into two components according to the Helmholtz decomposition; $\mathbf{u}_\gamma$ is the potential component resulting from the strain field and $\mathbf{u}_\omega$ is the solenoidal component, deduced from the vorticity distribution, through the Biot–Savart integral. The unperturbed stretched density gradient line is assumed to remain flat. The Biot–Savart Law then gives that the streamwise solenoidal velocity component u_ω, along the vorticity line, is zero. On the other hand, the strain field produces advection on the line $(u_\gamma.\partial u_\gamma/\partial x=\gamma^2 x)$. It also increases the density gradient while exponentially stretching the line $(g=g_0\exp(\gamma t))$. The advection, coupled with the density gradient, produces vorticity. Finally, the vorticity field is

$$\omega(x,t)=\gamma\frac{g_0}{\rho_0}x\sinh(\gamma t)+\omega_0. \tag{25}$$

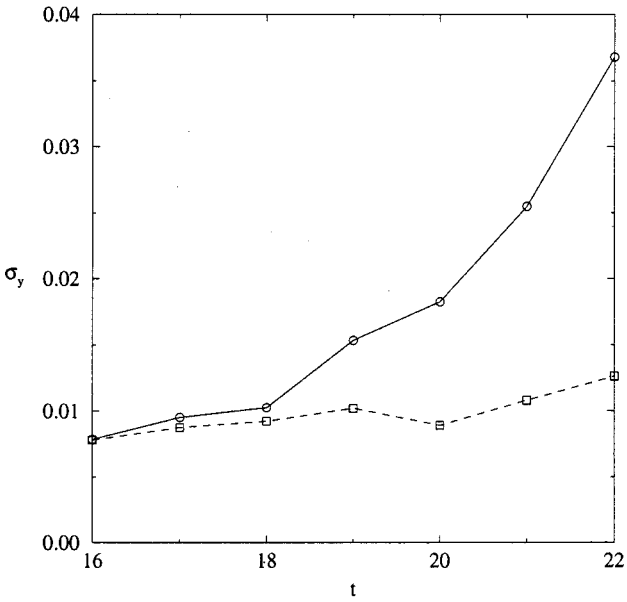

FIG. 16. Standard deviation σ_y of the oscillations of the central material line for run T3b: circles and solid line and T1b: squares and dashed line for $16<t<22$.

TABLE IV. Parameters of the truncated vorticity and density gradient filament simulation. A is the initial amplitude of the forcing.

Parameter	Value
X_{max}	82.5
H	16.5
h	0.15
δ	0.1875
dt	0.1
γ	0.15
g_0/ρ_0	4
A	0.04

It is seen that the vorticity distribution is linear which is consistent with the observed repartition of vorticity along the central isopycnic line of the temporal mixing layer in Fig. 4. At any $t>0$ the solution leads to infinite vorticity levels at $x\to\pm\infty$ and to a corresponding diverging solenoidal velocity field. However it gives a fair estimation of the vorticity production in the neighborhood of the saddle point ($x=0$) on a strained finite density gradient layer.

As quoted by Dritschel *et al.*,[10] the influence of the strain field is stabilizing. But, as seen from (25), it also produces intense vorticity which increases the receptivity of the layer to perturbations. Considering the ratio

$$\frac{\omega(x,t)}{\gamma}=\frac{g_0}{\rho_0}x\sinh(\gamma t)+\frac{\omega_0}{\gamma}, \tag{26}$$

it is seen that for $x<0$, the magnitude of the ratio increases with time as negative vorticity is enhanced (destabilizing effect). But due to the initial negative vorticity ω_0, the temporal evolution of the ratio is not monotonic for $x>0$. The magnitude of the ratio ω/γ decreases before reaching the minimum value of 0 at $t=-(1/\gamma)\mathrm{asinh}(\omega_0\rho_0/\gamma x g_0))$ (stabilizing effect), then starts to increase (destabilizing trend).

Meanwhile, according to the strain-vorticity competition stressed by Dritschel *et al.*,[10] at a given time, the layer is to be qualitively divided into three regions. On the left part of the layer, where vorticity can be arbitrarily high (depending on the x-section) the filament should break up into negative vorticity roll-ups. In the central region, where the ω/γ-ratio can be as weak as 0, the layer should be stabilized by the strain field. This stable region is, in fact, becoming thinner and thinner with time as baroclinic vorticity is enhanced on both sides of the saddle point of the strain field. Finally, on the right part, where vorticity exhibits high magnitude positive vorticity, the layer should also break up into counterclockwise rolling structures.

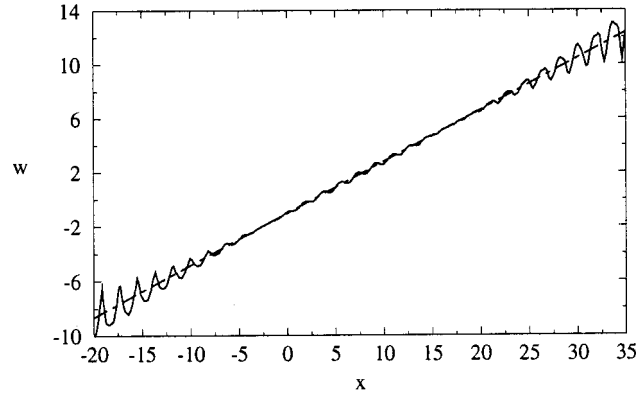

FIG. 17. Vorticity distribution along the strained, truncated vorticity, and density gradient layer (solid line) and comparison with the analytical prediction (dotted–dashed line) at $t=4$.

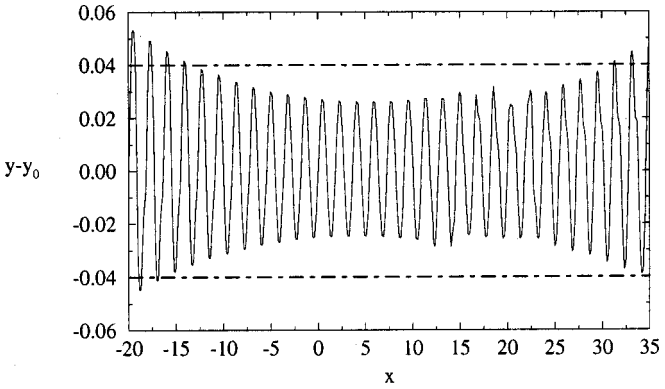

FIG. 18. Central part of the vorticity and density gradient filament at $t=4$ (solid line). Dotted–dashed lines represents the initial amplitude of the perturbation.

This model is subjected to a numerical computation. A forced, truncated negative vorticity and positive density gradient filament, initially aligned with the x-axis is placed in a uniform strain field. The filament is discretized as a single row of blob elements. This regularized approach of a single line of vorticity avoids the unphysical infinite amplification of perturbations of the vortex sheet as the wavelength of the disturbances collapses to zero, see Lundgren *et al.*[20] Then the cut-off parameter δ defines the width of the layer. The computational domain is defined by its length $2X_{max}$, and the

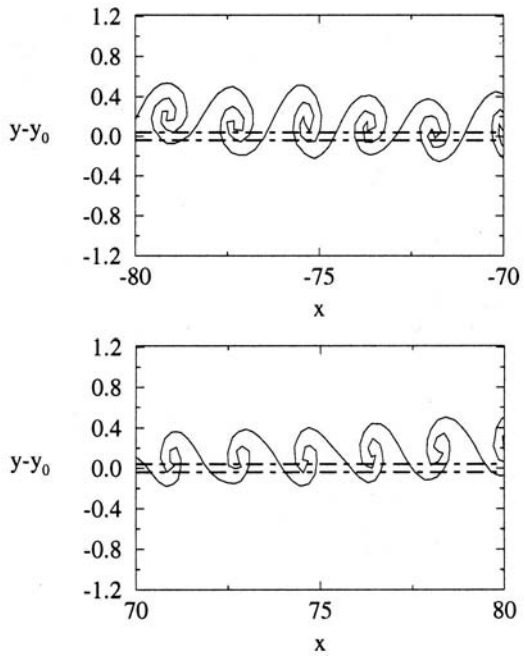

FIG. 19. The vorticity and density gradient filament at $t=4$ (solid line). Dotted–dashed lines represents the initial amplitude of the perturbation. Top: negative vorticity roll-ups. Bottom: positive vorticity roll-ups.

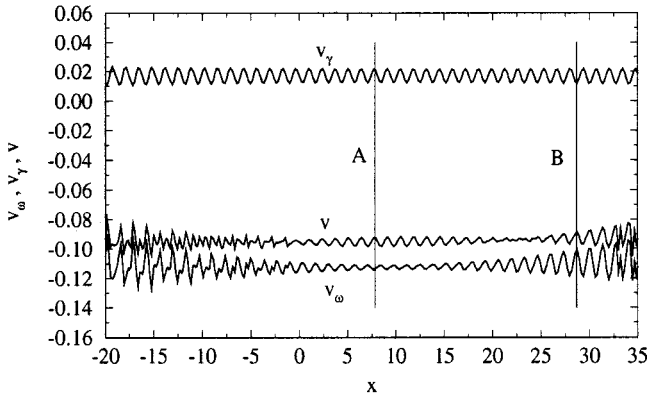

FIG. 20. Decomposition of the crosswise velocity v according to the solenoidal component v_ω and the potential component v_γ at $t=2$ in the central region of the layer.

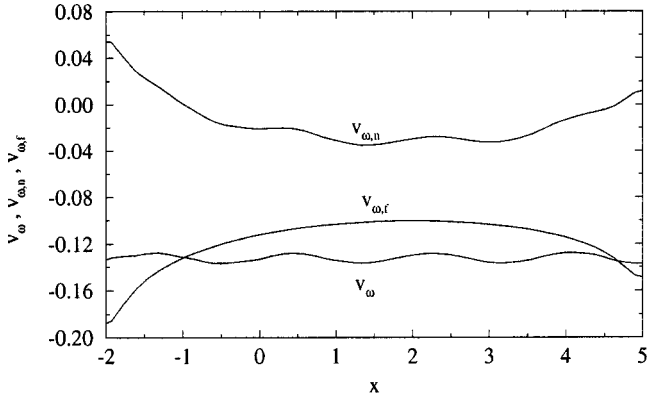

FIG. 22. Decomposition of the crosswise solenoidal velocity v_ω according to the near field $v_{\omega,n}$ and the far field $v_{\omega,f}$ at $t=4$.

elements advected beyond the boundaries of the domain ($\pm X_{\max}$) are deleted. Such a truncated line of vorticity tends naturally to rotate conformly to the circulation budget. Here, the crosswise component of the solenoidal field at a given crosswise distance is canceled which can be interpretated as a confinement of the layer between two slip-free walls. The height of the so-defined channel H is kept wider than the wavelength of the forcing to prevent any damping of the corresponding instabilities. The slip-free walls are modeled by the method of images as proposed and successfully applied by Inoue.[28] The images of the elements of the layer are placed symmetrically with respect to the walls and their vorticity is half of the one of the elements with opposite sign. The problem is normalized by the wavelength of the initial perturbation λ_0 and the magnitude of initial negative vorticity $|\omega_0|$.

The parameters of the computation are given in Table IV. The equations are solved using the RK2 scheme and the $K2$ cut-off function.

The vorticity distribution at $t=4$ along the line in the range $-20<x<35$ is compared to the analytical prediction 25 in Fig. 17. It is seen that the unforced analytical model accurately predicts the mean value of the vorticity distribution of the forced truncated layer.

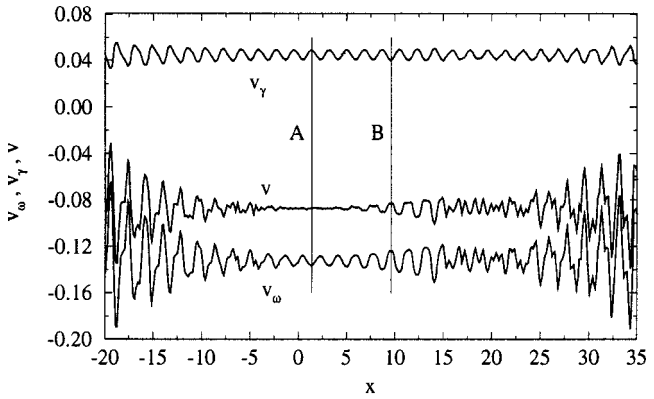

FIG. 21. Decomposition of the crosswise velocity v according to the solenoidal component v_ω and the potential component v_γ at $t=4$ in the central region of the layer.

The shape of the vorticity and density gradient filament at $t=4$ is seen in Figs. 18 and 19. The wavelength of the undulations is $\lambda(t=4)=\lambda_0 * \exp(\gamma t)=1.8$. In the central region, Fig. 18, the amplitude of the perturbation has decreased. On both the negative and positive vorticity region, Fig. 19, the layer is unstable. To analyze the stability properties of the layer, the crosswise velocity v is shown in Figs. 20 ($t=2$) and 21 ($t=4$) for the central region. It is shown that the solenoidal component v_ω and the potentiel component v_γ have opposite phases. The phase of the crosswise strain field is opposite to the one of the undulations of the layer (as it is $-\gamma y$) and tends to flatten them, while the vortical component is in phase with the perturbations thus working to amplify the undulations.

At $t=2$ the wavelength of the perturbation is $\lambda=1.35$. In Sec. A (see Fig. 20), corresponding to $x=7.8$ with $\omega=0.425=2.8\gamma$, the total velocity is in phase with the potential component v_γ so that the stabilizing effect of the strain field is stronger than the destabilizing effect of the solenoidal component; the magnitude of the perturbation is decreasing. On the contrary, in the section B, at $x=28.7$ with $\omega=4.24=28.3\gamma$, v is dominated by the solenoidal component v_ω so that the perturbation is amplified. It is concluded that, at $t=2$, within the range $-8<x<20$, corresponding to

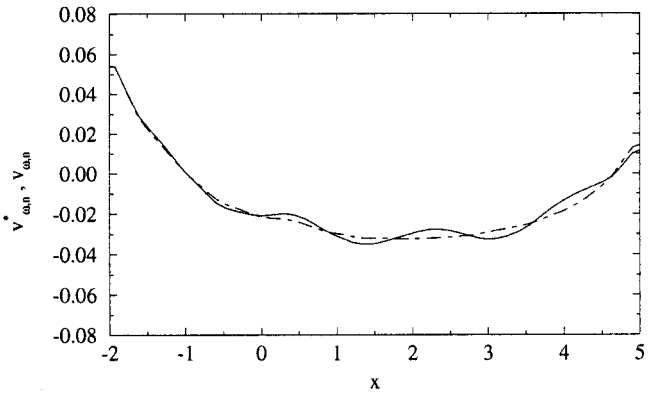

FIG. 23. Crosswise solenoidal velocity $v_{\omega,n}$ due to the near vorticity field ($-2<x<5$) (solid line) and comparison with the velocity induced by an analytical (unperturbed) vorticity distribution ($-2<x<5$) (dashed–dotted line) at $t=4$.

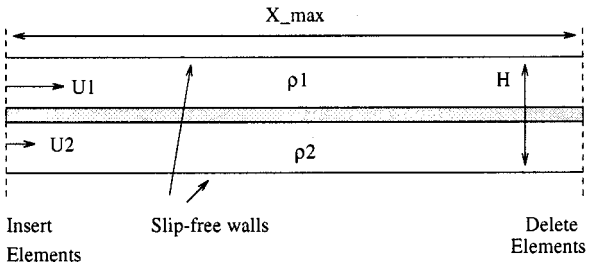

FIG. 24. Geometry of the spatial model.

$-16.4\gamma<\omega<17.7\gamma$, the layer is being stabilized, and that perturbations are developing outside of this range.

Later, at $t=4$, the stabilized region is expected to be thinner, because of the baroclinic production of vorticity. Section B clearly exhibits a vorticity driven crosswise velocity. The central part of the layer exhibits a neutral behavior to the perturbation (see section A). There, v exhibits a quasiconstant value of -0.086 within the range $-2<x<5$ corresponding to $-11.6\gamma<\omega<6\gamma$ so that perturbations are neither developing nor collapsing. The ratio ω to γ, characterizing the stability limit is surprisingly much lower than at $t=2$. The solenoidal component, of same order of magnitude as the potential component, actually prevents the strain field to stabilize the layer. The solenoidal component of the crosswise velocity is split into the near field $v_{\omega,n}$, due to the vorticity distribution for $-2<x<5$, and the far field $v_{\omega,f}$, induced by the vorticity outside of the region. The results are presented in Fig. 22 for $-2<x<5$. It is concluded that the solenoidal crosswise velocity fluctations are due to the near field. They result from a feedback effect of the perturbation (oscillations of the material layer) through the baroclinic torque. This is further demonstrated by comparing $v_{\omega,n}$ with the solenoidal field that would be induced by the unperturbed, analytical vorticity distribution along the oscillating material layer $v^*_{\omega,n}$ (see Fig. 23). It is concluded that the baroclinic torque not only increases the ratio ω to γ, destabilizing the layer but also promotes the fluctuations of the crosswise velocity through a perturbed vorticity source.

The present model illustrates the effects of a strain field on a vorticity and density gradient filament. The numerical simulation of the truncated layer clearly shows the competition between the stalibizing strain field and the destabilizing solenoidal field. It is concluded, in agreement with Dritschel *et al.*,[10] that the stability properties of such a filament are to be linked to the local γ to ω ratio and to the amplitude of the perturbation. Even in region where the ratio ω to γ is low, the baroclinic torque is a vorticity source sensitive to perturbations. These physical mechanisms are those triggering the baroclinic secondary instability.

IV. THE SPATIAL MODEL

A. Geometry and initial conditions

It has been shown that the temporal model is not able to capture the natural asymmetry of the flow due to inertial effects (even in the uniform-density case) because of the periodicity conditions imposed, see Corcos and Sherman[29] and Grinstein *et al.*[30] The evidence of the secondary baroclinic instability is now examined in the more realistic spatially developing two-dimensional mixing layer. The vorticity profile in the inlet section is Gaussian and the layer is confined between two slip-free walls. The computational domain is a vorticity layer truncated at a distance $X_{\max}$ of the splitter plate. The walls are modeled within a Schwartz–Christoffel conformal mapping of the physical space into the upper half plane. As proposed first by Ghoniem and Ng,[31] an appropriate system of images ensures a zero normal velocity at the walls. The elements are introduced in the computational domain respecting the Kutta condition. The downstream condition consists in deleting the elements as they cross the exit section of the computational domain. This assumption, though generating errors near the exit section, is commonly used in vortex methods.

The geometry of the configuration is given in Fig. 24. The layer is forced with the most unstable mode of the uniform density case and its first subharmonic. The signals are in phase, promoting the pairing of two main structures, see Corcos and Sherman.[29] The forcing signal corresponds, physically, to an oscillating splitter plate. The problem is normalized by the velocity scale U_1, the density ρ_1 of the top stream and the length scale H, height of the channel. The standard deviation σ of both the vorticity and the density gradient profiles at the inlet section is scaled so that $\sigma=H/(2\lambda)$ where λ is the most unstable wavelength of the uniform density case. This choice allows the pairing mode to appear without being constrained by the presence of the walls (Ghoniem and Ng[31]). The amplitude of the two forcing signals is 1.5% of H.

The equations are solved with the RK2 scheme and the cut-off function is $K2$. This reduction in the order of accuracy of the numerical schemes enhance the robustness of

TABLE V. Description of the computations for the investigation of the spatially developing mixing layer. The fifth column gives the number of isopycnic lines simulated. In all runs, the time step used is $dt=0.1$. In all cases the velocity ratio $r=U_2/U_1$ is 0.5. The asterisk indicates a simulation where a small scale perturbation is introduced. Its wavelength is the $H/20$ and its amplitude 1.5% of H.

Run	ρ_2/ρ_1	h	δ	iso.	$X_{\max}$
S.3a	1/3	0.0234	0.0273	7	5
S.3b	1/3	0.0234	0.0273	7	4
S.3c	1/3	0.0078	0.0091	21	4
S.3d*	1/3	0.0078	0.0091	21	3
S1a	1	0.0234	0.0273	7	5
S3a	3	0.0234	0.0273	7	5

TABLE VI. Spreading rates of the spatially developing, variable-density forced mixing layers with a velocity ratio $r=0.5$. Runs S.3a, S1a, S3a.

ρ_2/ρ_1	Δ'
1/3	0.119
1	0.116
3	0.070

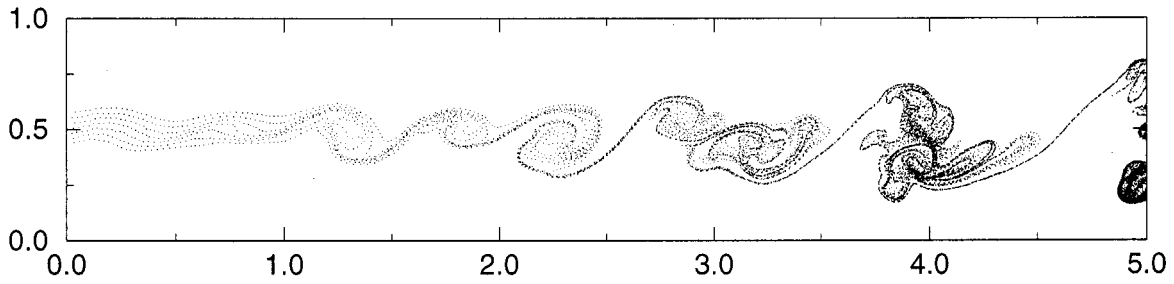

FIG. 25. Location of the elements at $t=8.0$ for a variable-density spatially developing shear layer with $U_2/U_1=0.5$ and $\rho_2/\rho_1=0.33$, $X_{\max}=5$, $h=0.0234$ (initial spatial step).

calculation in the region of intense gradients. The different runs are presented in Table V.

B. Numerical results

The dependence of the spreading rate Δ' on the density ratio is first investigated on the forced spatially developing mixing layer. Measurements are based on the analysis of time-averaged density profiles at different sections downstream of the splitter plate. For that reason, the low resolution simulations (runs S.3a, S1a, S3a) are used so that the computational cost per iteration remains low and a sufficient number of instantaneous density profiles can be averaged. The density thickness of the layer is defined as the crosswise distance where the averaged density departs from the free stream density by 1% of the density difference (a passive scalar is used for the uniform-density case). The density is reconstructed along four lines that are discretized with the spatial step $\delta y=0.01$ and placed at $x=1.5,2,3,4$. The spreading rate is then obtained by linear regression.

The results, presented in Table VI, are consistent with the previously published numerical investigation of Soteriou and Ghoniem,[11] where a detailed analysis of such a trend is developed. Again, the baroclinic torque is responsible for the distortions in the entrainment rate on both side of the layer, consequently changing its spreading rate.

The influence of the downstream boundary condition, i.e., the removal of the elements crossing the exit section of the computational domain, is investigated comparing instantaneous density profiles between two similar simulations with different length of the computational domain. This comparison, illustrated in Figs. 25 and 26, between the runs S.3a, where $X_{\max}=5$ and S.3b, where $X_{\max}=4$, at $t=8$ gives that the maximum difference between the density distributions $\rho(x,y)$ is less than 2% of the density difference for $x<X_{\max}-1$. It is concluded, in agreement with Soteriou and Ghoniem,[11] that the influence of the exit condition is significant only for $x>X_{\max}-1$. This statement allows us to reduce the length of the computational domain when focusing on phenomena expected to develop only a few distance downstream the trailing edge of the splitter plate.

The small scale break up of the braid is then investigated on rather highly spatially resolved simulations while the length of the computational domain is reduced to $X_{\max}=4$. The case considered is the case $s=1/3$ (run S.3c). The locations of the elements are shown at $t=8$ in Fig. 27. Conforming to what occurs in the temporal mixing layer, and to the conclusions of the simplified model, small scale structures are observed. It is then seen that the structure at $2<x<2.5$ exhibits a small scale roll-up where the vorticity has been intensified by the baroclinic torque. Moreover, along the right side braid of two next following primary structures, now pairing, a row of Kelvin–Helmholtz type structures is developing. The analysis of the undulations of the central isopycnic line is considered. The spectrum exhibits a main peak at $\lambda=0.2$ as seen from Fig. 28. The vorticity field within the square box $2.7<x<3.5$ and $0.1<y<0.9$ is reconstructed on a 256^2 Cartesian mesh. The isovorticity contours, presented in Fig. 29, show the small-scale structures of the destabilized braid. Besides, the core itself has broken up so that both the positive and negative vorticity are concentrated on small spots. The corresponding spatial instantaneous spectrum of enstrophy is given in Fig. 30. The result shows that the spectrum is continuous and exhibits enstrophy between the wave number $k=1$ and $k\sim 90$ corresponding to

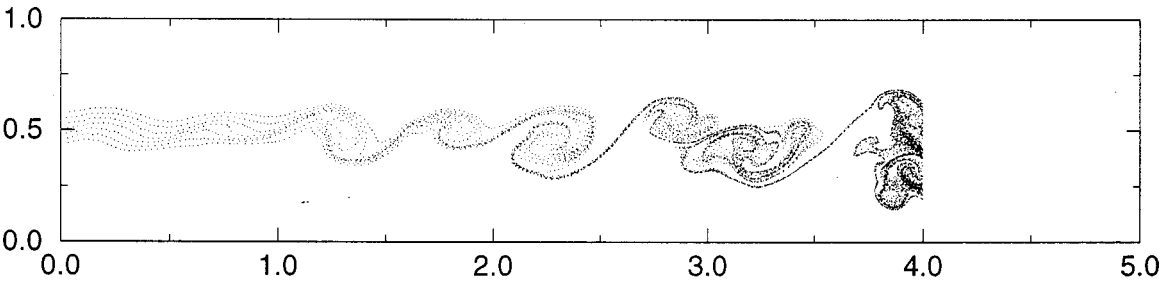

FIG. 26. Location of the elements at $t=8.0$ for a variable-density spatially developing shear layer with $U_2/U_1=0.5$ and $\rho_2/\rho_1=0.33$, $X_{\max}=4$, $h=0.0234$ (initial spatial step).

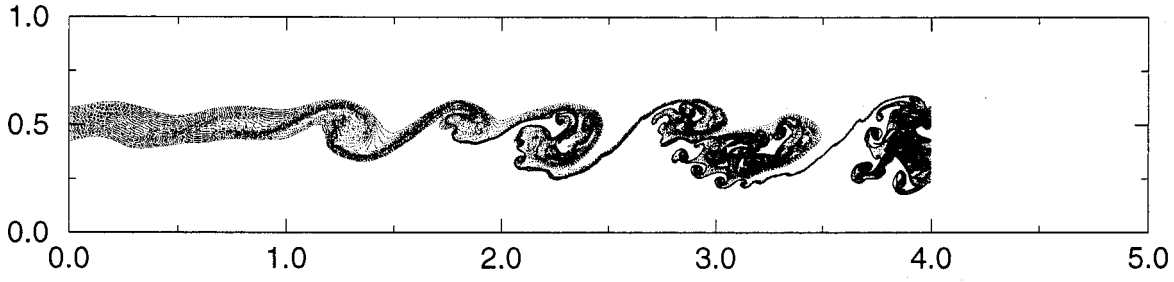

FIG. 27. Location of the elements at $t=8.0$ with $U_2/U_1=0.5$ and $\rho_2/\rho_1=0.33$, $X_{\max}=4$, $h=0.0078$ (initial spatial step).

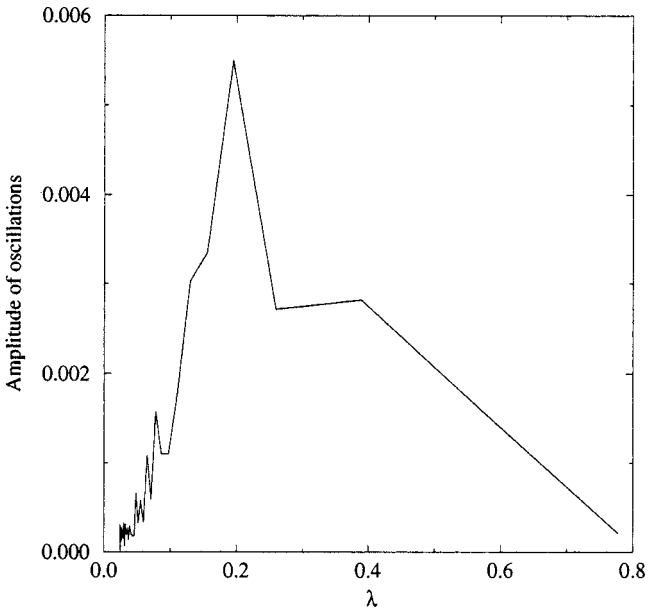

FIG. 28. Spectrum of oscillation of the braid $3.3<x<3.9$ of the spatially developing mixing, variable-density layer at $t=8$ (run S.3c).

the range of wavelength $\sim 0.009<\lambda<0.8$. The high wave number limit corresponds to the ''cut-off'' parameter δ. Three regions are identified. For the large scales $1<k<13$, the enstrophy is roughly uniformly repartitioned. Then for $13<k<30$, the slope of the enstrophy spectrum is found to be $k^{-2.75}$. Finally, the amount of enstrophy per wave number rapidly decreases with k and almost vanishes for $k>90$. It is then demonstrated that as soon as the first pairing, the baroclinic torque has drastically modified the topology of the vorticity map, creating a continuous spectral repartition of enstrophy.

Considering the vorticity field, even the first developed roll-up exhibits a right-side braid where small-scale instabilities are growing, see Fig. 31. An additional simulation, where a small-scale perturbation is introduced, is performed. The wavelength of the forcing is $H/20$ and its amplitude 0.15% of H, i.e., a tenth of the amplitude of the main mode and its first subharmonic (run S.3d*). The length of the computational domain has been reduced to $X_{\max}=3$ as the focus is on the first developed structure. The result presented in Fig. 32 suggests that the small-scale can be promoted and organized through an external low-amplitude high frequency forcing. It is suggested that the increased receptivity of the vorticity and density gradient braids can be used to favor the transition to turbulence, and to promote mixing.

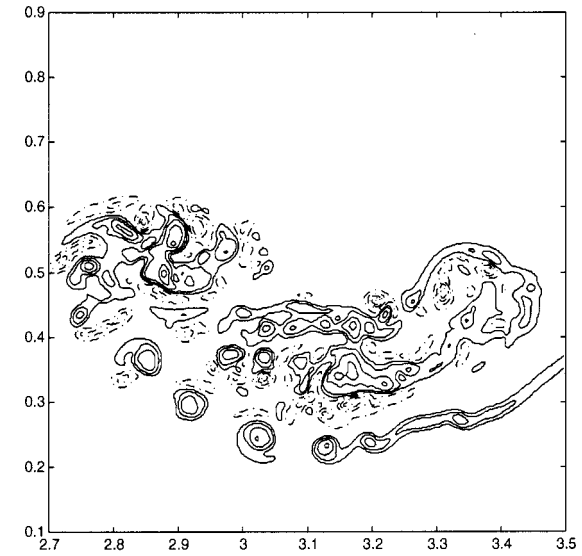

FIG. 29. Vorticity contours in the box $0.1<y<0.9$, $2.7<x<3.5$ at $t=8.0$ with $U_2/U_1=0.5$ and $\rho_2/\rho_1=0.33$, $X_{\max}=4$, $h=0.0078$ (initial spatial step).

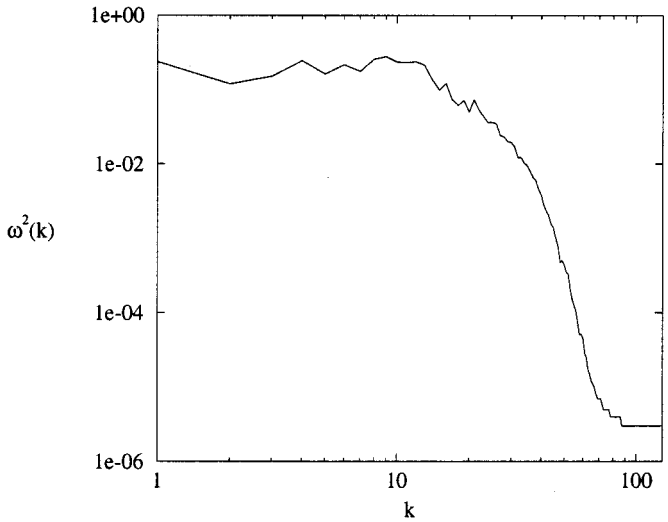

FIG. 30. Spectrum of enstrophy in the box $0.1<y<0.9$, $2.7<x<3.5$ at $t=8.0$ with $U_2/U_1=0.5$ and $\rho_2/\rho_1=0.33$, $X_{\max}=4$, $h=0.0078$ (initial spatial step).

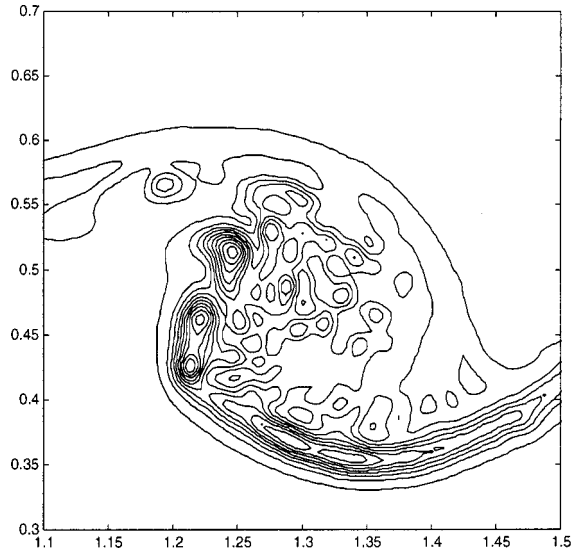

FIG. 31. Vorticity contours in the box $0.3<y<0.7$, $1.1<x<1.5$ at $t=8.0$ with $U_2/U_1=0.5$ and $\rho_2/\rho_1=0.33$, $X_{\max.}=4$, $h=0.0078$ (initial spatial step) run S.3c.

V. CONCLUSION

The present paper has shed some light on the small scale breaking-up of the two-dimensional, high Reynolds and Froude numbers, isovolume variable-density mixing layer. The secondary instability observed, both on the temporal and spatial model, appears in a vorticity enhanced braid. The basic mechanisms rely on the baroclinic production of vorticity that takes place on the braids linking the primary Kelvin–Helmholtz structures. This vorticity production is, itself, the result of the coupling of the density gradient and the advection of the fluid from the braids toward the vortical cores. Contrary to the secondary instability previously described at the saddle point of the gravity-dominated, stratified, shear layers, secondary roll-ups emerge on the curved light-side vorticity braid. The difference lies on the nature of the pressure gradient which is fixed in direction and intensity in the buoyancy-driven case while it results from acceleration field in the high Reynolds and Froude numbers mixing layer, studied here. Then, the analysis of a simplified model of a stretched density-gradient and vorticity filament, modeling the braid of the mixing layer, stressed that the baroclinic torque amplifies the magnitude of the vorticity. Consequently, the solenoidal field, that tends to amplify perturbations within the vorticity filament, can compete with the stabilizing strain field. Moreover, the perturbations induce fluctuations on the baroclinic torque, yielding a perturbed vorticity source. This feedback effect of the perturbation through the baroclinic torque also leads toward the destabilization. It is concluded that the density stratification not only changes the global evolution of the flow, such as its spreading rate but also should speed up the transition to turbulence of high Reynolds number spatially developing mixing layers. Such observations suggest that high frequency external forcing of the variable-density shear layer could be an efficient active control strategy to enhance the mixing rate.

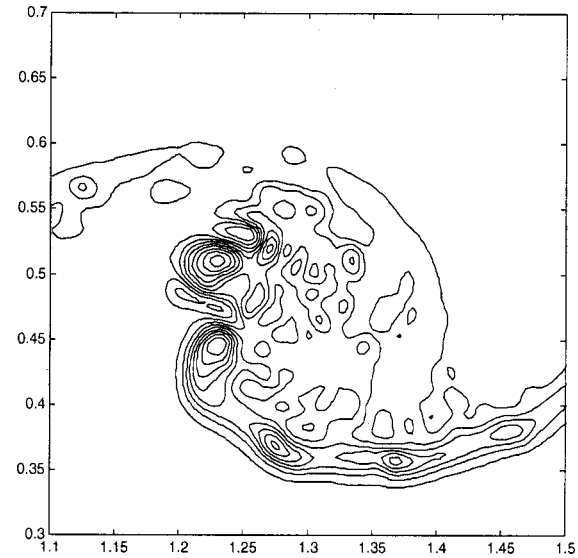

FIG. 32. Vorticity contours in the box $0.3<y<0.7$, $1.1<x<1.5$ at $t=8.0$ with $U_2/U_1=0.5$ and $\rho_2/\rho_1=0.33$, $X_{\max}=4$, $h=0.0078$ (initial spatial step) run S.3d*.

ACKNOWLEDGMENTS

This work is supported by the Délégation Générale pour l'Armement (DGA/DSP). We acknowledge the CINES, Centre Informatique National de l'Enseignement Supérieur for computational facilities.

[1] J. S. Turner, *Buoyancy Effects in Fluids* (Cambridge University Press, Cambridge, 1973).
[2] G. L. Brown and A. Roshko, ''On density effects and large structure in turbulent mixing layers,'' J. Fluid Mech. **64**, 775 (1974).
[3] J. H. Konrad, ''An experimental investigation of mixing in two-dimensional turbulent shear flows with applications to diffusion-limited chemical reactions,'' Ph.D. thesis, California Institute of Technology, 1976.
[4] S. Lele, ''D.n.s. of compressible free shear flows,'' CRT Report No. N89-22827, 1989.
[5] C. Staquet, ''Two-dimensional secondary instabilities in a strongly stratified shear layer,'' J. Fluid Mech. **296**, 73 (1995).
[6] D. B. Altman, ''Critical layers in accelerating two-layer flows,'' J. Fluid Mech. **197**, 429 (1988).
[7] G. M. Corcos and F. S. Sherman, ''Vorticity concentration and the dynamics of unstable free shear layers,'' J. Fluid Mech. **73**, 241 (1976).
[8] S. A. Thorpe, ''A method of producing a shear flow in a stratified fluid,'' J. Fluid Mech. **32**, 693 (1968).
[9] S. A. Thorpe, ''Transitional phenomena on turbulence in stratified fluids,'' J. Geophys. Res., [Oceans] **92**, 5231 (1987).
[10] D. G. Dritschel, P. H. Haynes, M. N. Juckes, and T. G. Sheperd, ''The stability of a two-dimensional vorticity filament under uniform strain,'' J. Fluid Mech. **230**, 647 (1991).
[11] M. C. Soteriou and A. F. Ghoniem, ''Effects of the free-stream density ratio on free and forced spatially developing shear layers,'' Phys. Fluids A **7**, 2036 (1995).
[12] P. Dimotakis, ''Two-dimensional shear-layer entrainment,'' AIAA J. **24**, 1791 (1986).
[13] C. R. Anderson, ''Vortex methods for flows of variable density,'' Lawrence Berkeley Laboratory Report No. LbL-16702 (Ph.D. thesis, 1983).
[14] A. Ghoniem, G. Heidarinejad, and A. Krishnan, ''Numerical simulation of a thermally stratified shear layer using the vortex element method,'' J. Comput. Phys. **79**, 135 (1988).
[15] E. G. Puckett, ''Vortex methods an introduction and survey of selected research topics,'' in *Incompressible Computational Fluid Mechanics*, edited by R. Nicolaides and M. Ginzburger (Cambridge University Press, Cambridge, 1992).

[16]M. C. Soteriou, ''Numerical study of turbulent combustion in a shear layer,'' Ph.D. thesis, Massachusetts Institute of Technology, Cambridge, MA, 1993.
[17]A. Michalke, ''On spatially growing disturbances in an inviscid shear layer,'' J. Fluid Mech. **23**, 521 (1965).
[18]G. L. Brown, ''The entrainment and large structure in turbulent mixing layer,'' in *Proceedings of the Fifth Australasian Conference on Hydraulics and Fluid Mechanics*, 1974, pp. 353–359.
[19]A. J. Chorin, ''Numerical study of slightly viscous flow,'' J. Fluid Mech. **57**, 785 (1973).
[20]T. S. Lundgren, J. Yao, and N. N. Mansour, ''Microburst modeling and scaling,'' J. Fluid Mech. **239**, 461 (1992).
[21]J. T. Beale and A. Majda, ''High order accurate vortex methods with explicit velocity kernels,'' J. Comput. Phys. **58**, 188 (1985).
[22]G. Heidarinejad, ''Vortex simulation of the reacting shear layer,'' Ph.D. thesis, Massachusetts Institute of Technology, Cambridge, MA, 1989.
[23]A. Leonard, ''Vortex methods for flow simulation,'' J. Comput. Phys. **37**, 289 (1980).
[24]M. M. Rogers and R. D. Moser, ''The three-dimensional evolution of a plane mixing layer: The Kelvin–Helmholtz rollup,'' J. Fluid Mech. **243**, 183 (1992).
[25]R. W. Metcalfe, S. A. Orszag, M. E. Brachet, S. Menon, and J. J. Riley, ''Secondary instability of a temporally growing mixing layer,'' J. Fluid Mech. **184**, 207 (1987).
[26]A. Michalke, ''On the inviscid instability of the hyperbolic tangent velocity profile,'' J. Fluid Mech. **19**, 543 (1964).
[27]J. Reinaud, L. Joly, and P. Chassaing, ''Numerical simulation of a variable-density mixing layer,'' ESAIM Proceedings, 1999, Vol. 7 (http://www.emath.fr/Maths/Proc/Vol.7/index/html).
[28]O. Inoue, ''Vortex simulation of turbulent mixing layers,'' AIAA J. **23**, 367 (1985).
[29]G. M. Corcos and F. S. Sherman, ''The mixing layer: Deterministic models of a turbulent flow. Part 1. Introduction and the two-dimensional flow,'' J. Fluid Mech. **139**, 29 (1984).
[30]F. F. Grinstein, E. S. Oran, and J. P. Boris, ''Numerical simulations of asymmetric mixing in planar shear flows,'' J. Fluid Mech. **165**, 201 (1986).
[31]A. F. Ghoniem and K. K. Ng, ''Numerical study of the dynamics of a forced shear layer,'' Phys. Fluids **30**, 706 (1987).